

FIG. 2. Charge sensitive molecular vibrations of κ -(BEDT-TTF) $_2$ Hg(SCN) $_2$ X (X=Br,Cl). For κ -(BEDT-TTF) $_2$ Hg(SCN) $_2$ Br: (a) Raman scattering spectra under 0.4% tensile strain along the c-axis, the (b) frequency and (c) full-width-half-maximum (FWHM) of ν_2 without strain from Ref. [3], and the (d) frequency and (e) full-width-half-maximum (FWHM) of ν_2 under 0.4% tensile strain along the c-axis. For κ -(BEDT-TTF) $_2$ Hg(SCN) $_2$ Cl: (f) Raman scattering spectra of under 1.6% tensile strain along the b-axis, the (g) frequency and (h) full-width-half-maximum (FWHM) of ν_2 under 1.6% tensile strain along the b-axis, and the (i) frequency and (j) full-width-half-maximum (FWHM) of ν_2 without strain from Ref. [8].

at lowest temperatures [8] that is insensitive to magnetic field [19]. The chemical tuning of charge order motivates this study of controlling the charge order transition by tuning interactions through the application of uniaxial strain.

In recent years, strain tuning has been established as an ideal method for control of many body quantum systems. To explore the variety of materials and physics which can be studied under strain, many recent advancements have been made in the methods and devices for strain application [20, 21]. Band structure [22, 23] and band topology [24, 25] have been successfully tuned under strain. Moreover, magnetic ground states [26] have been reversibly tuned under uniaxial strain. Competing interactions have been studied under strain, such as the competition between nematicity and superconductivity [27–30]. While these studies have established strain as a key tuning parameter for electronic phase transitions, the ability to transform the electronic ground state across a phase boundary in both directions remains to be realized.

In this letter, we demonstrate experimental evidence of tuning the ground state of κ -Hg-X via uniaxial strain across the phase border in two directions, *in* and *out* of the charge ordered state. We experimentally observe softening of collective dipole fluctuations through the

dimer Mott insulator to charge order insulator transition, suggesting collective behavior drives the transition. Our results demonstrate the tuning of ground states of strongly correlated electron systems and serve as a foundation for tuning collective behavior of multiferroic materials.

Experimental Procedure— Due to the large mismatch in the thermal expansion of ET-based materials when compared to metals such as Cu [31, 32], we apply thermal strain by gluing to a Cu substrate. Strain is applied by gluing the sample on opposite ends of the crystal axis, which contracts according to the thermal contraction of Cu on cooling. Temperature-dependent structural parameters for κ -Hg-Br are presented in the Supplementary Material [32]. For κ -Hg-Cl temperature-dependent parameters of the structure published in Ref. [18] were used. We calculate the temperature-dependent strain, which we expect to be constant below 100 K. Raman scattering spectroscopy is used to measure molecular vibrations, lattice phonons, and collective dipole fluctuations. The detailed experimental methods are provided in the Supplementary Material [32].

Detecting Charge Order from Molecular vibrations— Charge order in the κ -(ET) $_2$ X salts corresponds to an unequal distribution of charge between the individual ET molecules within (ET) $_2^{1+}$ dimers. As shown in Fig. 1,

when the distribution of the highest occupied molecular orbital (HOMO) is equal ($n_a = n_b = 0.5$) the electronic system is in the dimer Mott phase, and when the HOMO is unequally distributed ($n_a \neq n_b$) the system is said to be in the charge order phase. To measure the charge of each ET molecule, we use charge sensitive molecular vibrations. The frequency of the Raman active molecular vibration ν_2 is linear with site charge n as follows [33]:

$$\omega(n) = 1447 + 120 \frac{\text{cm}^{-1}}{e} (1 - n) \quad (1)$$

A splitting of the line shape of the molecular vibration ν_2 into two distinct Lorentzian profiles with a frequency difference of $\Delta\omega$ corresponds to a charge ordered state with charge separation of

$$\Delta n = |n_a - n_b| = \frac{\Delta\omega}{120 \text{ cm}^{-1}} e \quad (2)$$

Previous studies of κ -Hg-Br at ambient pressure have demonstrated that no splitting of ν_2 is observed down to lowest temperatures (Fig. 2(b)), consistent with the dimer Mott phase. Broadening of the lineshape on cooling points towards charge fluctuations and places this material close to the charge ordered phase in the phase diagram (Fig. 2(c)) [3]. In this work we examine the charge state of κ -Hg-Br under a tensile strain of 0.4% along the c axis. We show the Raman spectra of molecular vibrations of κ -Hg-Br under strain as a function of temperature in Fig. 2(a). We observe a striking result: the charge sensitive molecular vibration ν_2 splits below $T_{\text{CO}}=33$ K, indicating the charge order transition. This temperature is slightly above $T_{\text{CO}}=30$ K for Hg-Cl [17]. We estimate the charge separation using two methods of lineshape analysis. First, we consider independent Lorentzian profiles that correspond to a static charge order. We plot the frequencies of each site and the corresponding molecular charge in Fig. 2(d). We find that in the static case, the charge separation is $0.28e$, slightly larger than $0.2e$ found for Hg-Cl in the CO phase [8, 17]. The linewidth of ν_2 can be used as a tool to analyze the temperature dependence of charge fluctuations near the charge order transition. We compare the linewidth of ν_2 with and without strain. Without strain (Fig. 2(c)) the linewidth increases below 40 K and remains broad down to lowest temperatures, suggesting the presence of strong fluctuations [3]. Under strain (Fig. 2(e)) the linewidth increases below 60 K and abruptly decreases below the charge order transition at 33 K, suggesting a freezing out of fluctuations.

For κ -Hg-Cl at ambient pressure a splitting of ν_2 is observed at 30 K (Fig. 2(i)), consistent with the charge order phase [3]. We examine the ground state of κ -Hg-Cl under a tensile strain of 1.6% along the b axis. As shown in the temperature dependent Raman spectra of κ -Hg-Cl under strain (Fig. 2(f)), we do not observe a

splitting of ν_2 down to 11 K. At $T_{\text{CO}}=11$ K, where ν_2 finally splits, we observe 3 distinct peaks. We can therefore claim that we have suppressed the charge order transition to 10 K, far below $T_{\text{CO}}=30$ K in the normal state [17]. It is interesting to note the inhomogeneity of the spectra, demonstrating that a fraction of the dimer sites are still in the dimer Mott phase. We plot the estimation of molecular charge in Fig. 2(g). This leads to an estimated charge separation of $0.32e$ within charge ordered dimers. We compare the linewidth of ν_2 through the charge order transition, with and without strain. Without strain (Fig. 2(j)) the linewidth increases above the transition and then drops significantly below the charge order transition, denoting a static order [8]. Under strain (Fig. 2(h)) the linewidth begins to increase at 25 K, above the transition; however, the linewidth does not significantly decrease below the charge order transition, suggesting fluctuations persist below the transition.

To summarize, we have successfully tuned the quantum dipole liquid candidate κ -Hg-Br into a charge ordered state below 33 K, inducing charge order, and we have successfully tuned the charged order insulator κ -Hg-Cl into a mixed state below 10 K, suppressing charge order. This establishes we have tuned in both directions across the phase border through application of uniaxial strain.

Collective dipole fluctuations—Under ambient pressure, κ -Hg-Br undergoes a metal-insulator transition at 80 K to the dimer Mott phase [34]. In the Mott insulating phase for this material, charge fluctuations are observed as characterized by the linewidth of ν_2 , corresponding to fluctuations of electric dipoles on $(\text{ET})_2^{1+}$ lattice sites. These dipole fluctuations were shown to be a collective effect, resulting in a collective excitation, which behaves as a soft mode. Unlike soft modes of displacement type ferroelectrics, this mode does not correspond to lattice vibrations. A mode corresponding to collective fluctuations of charge within $(\text{ET})_2^{1+}$ dimer lattice sites was predicted theoretically: It is expected to behave as a soft mode on approaching a charge order transition, and appearing at finite frequency in the ordered state [35]. This mode was also detected experimentally in the Raman scattering spectra of κ -Hg-Br at ambient strain at around 50 cm^{-1} , consistent with dipole liquid behavior [3, 36].

We examine the Raman spectra of κ -Hg-Br under strain in the low frequency region below 200 cm^{-1} , which corresponds to the frequency of collective dipole fluctuations. We plot the temperature dependent Raman spectra of κ -Hg-Br in the (b,b) polarization with phonons subtracted in Fig. 3(a) (for the spectra without phonons subtracted see inset). At temperatures below 80 K we observe a broad mode in this range, softening through the strain-induced charge order transition. We fit this broad feature to a Lorentzian oscillator and plot the temperature dependence of the fitted frequency in Fig. 4. At 37 K the broad mode is centered around 50 cm^{-1} . Be-

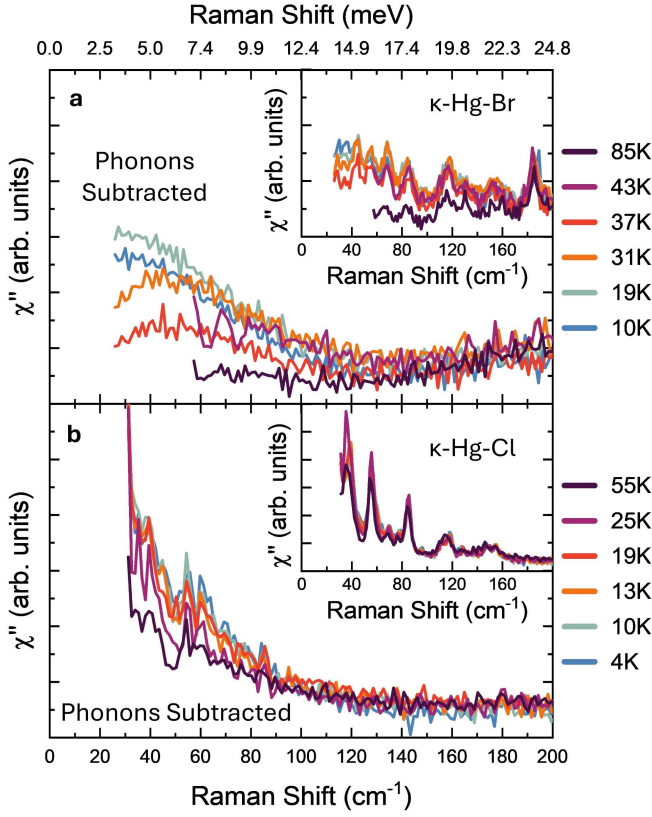


FIG. 3. Low frequency Raman scattering spectra of (a) κ -(BEDT-TTF) $_2$ Hg(SCN) $_2$ Br in the (b,b) polarization and (b) κ -(BEDT-TTF) $_2$ Hg(SCN) $_2$ Cl in the (c,c) polarization. Each spectra is shown with phonons subtracted. Spectra without phonons subtracted are shown in the insets.

low 37 K down to 19 K, the spectral weight shifts to lower frequencies, down to 30 cm^{-1} . The fit suggests a slight shift to higher frequencies at 10 K. As shown in the inset of Fig. 4, there is also an increase in the integrated intensity of the dipole fluctuations mode on cooling, with a maximum at 14 K. The shift of spectral weight to lower frequencies is consistent with a behavior of soft mode of collective dipole fluctuations through the charge order phase transition. The sudden decrease in integrated intensity below the phase transition suggests a renormalization of the spectral weight of the collective dipole fluctuations.

In the absence of strain, κ -Hg-Cl undergoes a metal to charge order insulator transition at $T_{\text{CO}}=30 \text{ K}$ [17], where collective dipole fluctuations are not observed [12]. We plot the low frequency Raman spectra of κ -Hg-Cl under strain, where $T_{\text{CO}}=11 \text{ K}$, with phonons subtracted in the (c,c) polarization in Fig. 3(b) (for the spectra without phonons subtracted see inset). While the presence of the elastic line precludes us from going to low frequencies, the changes in the observed range are negligible.

Discussion— Below we use calculations on the extended Hubbard model to understand the effect of strain

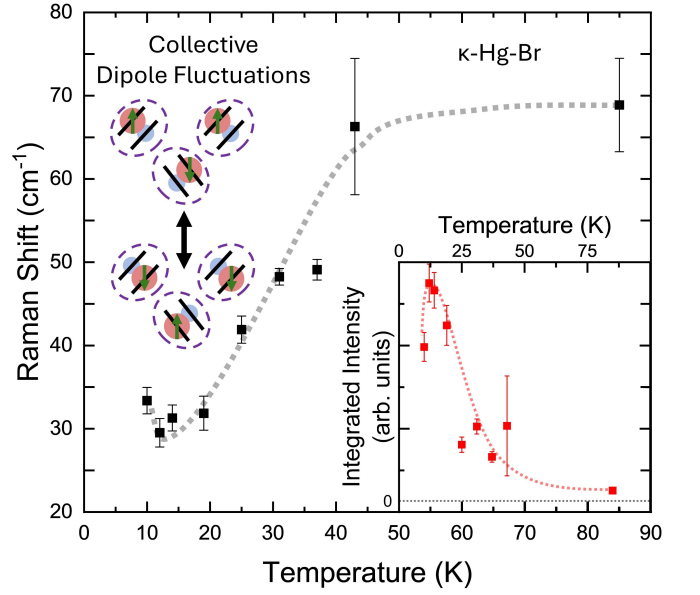


FIG. 4. Fitted resonant frequency of collective dipole fluctuations in κ -(BEDT-TTF) $_2$ Hg(SCN) $_2$ Br. (Inset) Integrated Intensity of the fit. Dashed lines are guides to the eye.

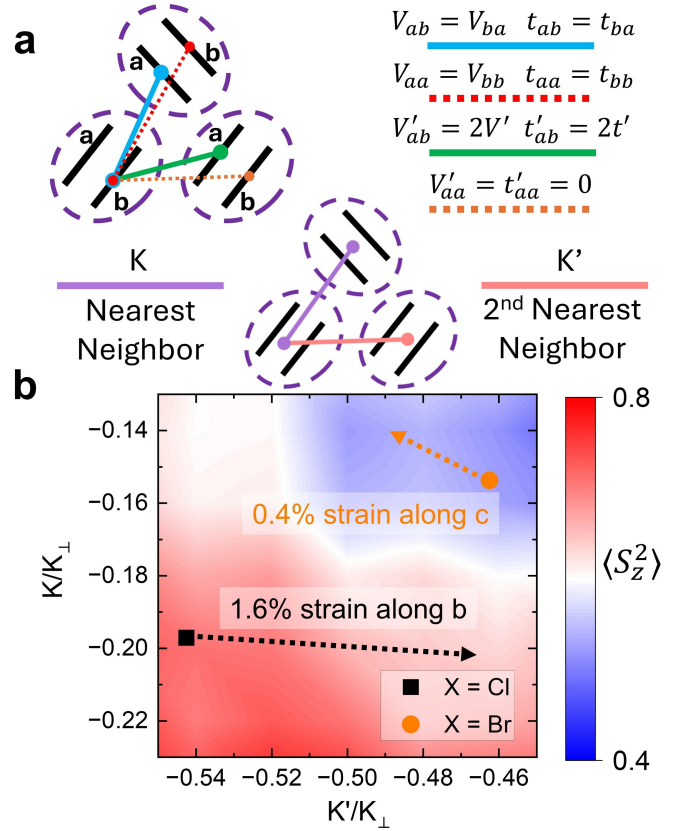


FIG. 5. **a** Interaction scheme of the Transverse Field Ising Model (TFIM). **b** Phase Diagram of TFIM parameters from Ref. [37], with $\langle S_z^2 \rangle$ estimated via Monte Carlo Simulation.

on the ground state of the studied materials. Correlated electron physics phenomena in κ -(ET)₂X is best understood through the extended Hubbard model [1, 2, 5]. This model includes intradimer interactions as well as interdimer interactions. The intradimer interactions include intramolecular electron-electron repulsion U , intradimer hopping t_d , and intradimer electron-electron repulsion V_d , which are renormalized to U_{eff} . When the intradimer hopping t_d is strong enough, the correlated electron system becomes $\frac{1}{2}$ -filled in the dimer Mott phase. The extended Hubbard model is then written as follows:

$$H_1 = U_{\text{eff}} \sum_{\text{sites } i} n_{i\uparrow} n_{i\downarrow} + \sum_{i \neq j} V^{ij} (n_{i\uparrow} + n_{i\downarrow})(n_{j\uparrow} + n_{j\downarrow}) - \sum_{i \neq j} \sum_{\text{Spin } \sigma} t^{ij} (c_{i\sigma}^\dagger c_{j\sigma} + \text{h.c.}) \quad (3)$$

where V and V' correspond to electron repulsion between nearest neighboring and second nearest neighboring (ET)₂¹⁺ dimer sites, respectively. Likewise, t and t' correspond to charge transfer between nearest neighboring and second nearest neighboring (ET)₂¹⁺ dimer sites.

Theoretical predictions using the extended Hubbard and Kugel-Khomskii Models [1, 2, 35, 37] parameterize the charge order transition in terms of competition between interdimer electron repulsion, V , and intradimer charge transfer, t_d : The transition into the charge ordered state is driven by the decrease of dimerization t_d relative to interdimer electronic repulsion V . Following Ref. [1, 2, 37] the emergent charge dipoles on dimer sites can be mapped onto Ising-like dipoles represented by $S = 1$ spins and subsequently modeled by the $S = 1$ transverse field Ising model (TFIM):

$$\hat{H} = K_\perp \sum_i \hat{S}_i^x + \frac{1}{2} \sum_{i \neq j} K^{ij} \hat{S}_i^z \hat{S}_j^z \quad (4)$$

Where $K_\perp = 2t_d$ is the effective transverse field and K^{ij} is the coupling between electric dipoles that are represented as $S = 1$ spins. The coupling between electric dipoles on nearest neighboring (ET)₂¹⁺ lattice sites is parametrized by K and the coupling between second nearest neighbors is parametrized by K' (see Fig. 5a), analogous to electron repulsion between nearest (V) and second nearest (V') neighboring (ET)₂¹⁺ dimer sites. The exact form of the K^{ij} is written in the supplementary material [32], but the dependence of the K^{ij} on the monomer interactions (see Fig. 5) is as follows:

$$K^{ij} \propto V_{aa}^{ij} - V_{ab}^{ij} + \frac{(t_{aa}^{ij})^2 - (t_{ab}^{ij})^2}{V_d} \quad (5)$$

It is important to note that K^{ij} correspond to differences of the interdimer interactions between the a and b molecules within (ET)₂¹⁺ dimer sites, as shown in Fig. 5. The nearest neighbor interactions (t, V) are stronger than

the second-nearest neighbor interactions (t', V'); however, the differences in these interactions between the a and b molecules are much larger for the second-nearest neighbor interactions [37, 38]. For κ -Hg-Br and κ -Hg-Cl, the interactions between second-nearest neighbors (K') are expected to be twice as strong as nearest neighbors (K) [37], which is a region of parameter-space that lacks thorough investigation. We therefore turn to a careful analysis of the tuning of the TFIM parameters under strain, using the monomer interactions from the extended Hubbard model. Using the crystallographic structure of κ -Hg-X and its changes with the application of strain, we calculate and plot the tuning of the TFIM parameters in Fig. 5b. We perform a Monte Carlo simulation of the TFIM in order to evaluate the expectation value of $\langle \hat{S}_z^2 \rangle$, which corresponds to the spontaneous electric dipole moment presented in the phase diagram in Fig. 5b. For a detailed description of the analysis of the extended Hubbard model and TFIM under strain, see the Supplementary Material [32].

Our analysis shows that under strain the second-nearest neighbor interaction K' undergoes substantial tuning when compared to the nearest neighbor interaction K . $K_\perp = 2t_d$ does not lie entirely along one axis, but it is expected that tensile strain along either axis will slightly decrease t_d . Application of tensile strain on κ -Hg-Br along c -axis leads to an increase of the $|K'/K_\perp|$ ratio, driving a larger expectation value of $\langle S_z^2 \rangle$, which means that charge order becomes more energetically favorable. Application of tensile strain on κ -Hg-Cl along b -axis leads to a decrease of the $|K'/K_\perp|$ ratio, leading to a smaller expectation value of $\langle S_z^2 \rangle$, and indicating that charge order becomes less energetically favorable. This analysis demonstrates that for the κ -Hg-X materials under strain, the charge order transition is driven largely by the competition between $K_\perp \propto t_d$ and K' , which is parametrized by interactions projected entirely onto the b -axis, namely V' . The compressive strain along b -axis strengthens $K' \propto V'$ and tensile strain along b -axis weakens $K' \propto V'$.

We therefore conclude that charge order in κ -Hg-X salts is tuned through the ratio of V'/t_d , as shown in Fig. 6. This tuning allows us to observe the dynamics of the soft mode around the charge order phase transition. As the charge order transition is approached in the dimer Mott phase, the collective mode of charge fluctuations is expected to soften [35]. Moreover, calculations from Ref. [35] demonstrate that the collective mode is expected to soften to a finite frequency at the charge order transition rather than to zero frequency. Our observation of the softening of the collective dipole fluctuations in κ -Hg-Br through the charge order transition (see Fig. 3) is in strong agreement with theoretical predictions [1, 2, 35].

Conclusion—We provide experimental evidence of tuning triangular lattice Mott insulators κ -(BEDT-TTF)₂X materials in both directions across the charge order phase

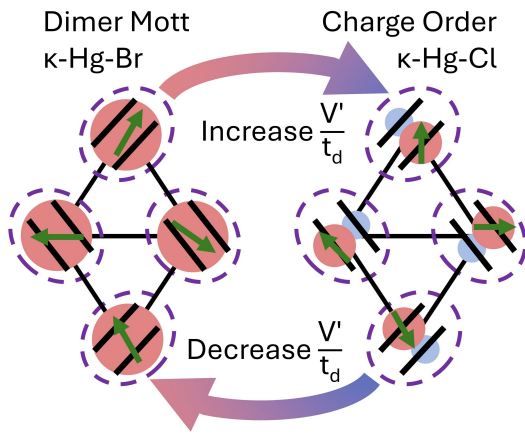


FIG. 6. Tuning of charge order in κ -(BEDT-TTF) $_2$ Hg(SCN) $_2$ X (X=Br, Cl). The tuning of the ratio V'/t_d is suggested as a pathway for control the charge order phase transition.

transition by uniaxial strain. We induced charge order in the Dipole-Liquid κ -Hg-Br at 33 K by application of 0.4% strain along c -axis, and suppressed charge order in the Dipole-Solid κ -Hg-Cl from 30 K down to 11 K by an application of the 1.6 % uniaxial strain along b -axis. Our calculations based on the estimate of the change of structural parameters with strain and using Transverse Ising Model to estimate charge order establishes a mechanism to control charge order via strain in all κ -(ET) $_2$ X materials by tuning the ratio of $\frac{V'}{t_d}$.

We establish the control of electronic ferroelectricity through modification of competing interactions of emergent electric dipoles. We hope that our work will serve as a foundation for tuning multiferroic materials with an optimistic outlook for switching behavior of multiple degrees of freedom.

Acknowledgements— The authorst thank S. Ghosh, B. Powell, and S. Winter for fruitful discussions. The work at JHU was supported by NSF Award No. DMR-2004074.

[1] Hotta, C. Quantum electric dipoles in spin-liquid dimer mott insulator κ -ET $_2$ Cu $_2$ (CN) $_3$. *Physical Review B* **82**, 241104(R) (2010). URL <https://link.aps.org/doi/10.1103/PhysRevB.82.241104>.

[2] Naka, M. & Ishihara, S. Electronic ferroelectricity in a dimer mott insulator. *Journal of the Physical Society of Japan* **79**, 063707 (2010). URL <https://doi.org/10.1143/JPSJ.79.063707>.

[3] Hassan, N. *et al.* Evidence for a quantum dipole liquid state in an organic quasi-two-dimensional material. *Science* **360**, 1101–1104 (2018). URL <https://www.science.org/doi/abs/10.1126/science.aan6286>.

[4] BEDT-TTF refers to (bisethylenedithio)tetrathiafulvalene.

[5] Dayal, S., Clay, R. T., Li, H. & Mazumdar, S. Paired

electron crystal: Order from frustration in the quarter-filled band. *Phys. Rev. B* **83**, 245106 (2011). URL <http://link.aps.org/doi/10.1103/PhysRevB.83.245106>.

[6] Nakamura, K., Yoshimoto, Y., Kosugi, T., Arita, R. & Imada, M. Ab initio derivation of low-energy model for κ -ET type organic conductors. *Journal of the Physical Society of Japan* **78**, 083710 (2009). URL <https://doi.org/10.1143/JPSJ.78.083710>. URL <https://doi.org/10.1143/JPSJ.78.083710>.

[7] Kandpal, H. C., Opahle, I., Zhang, Y.-Z., Jeschke, H. O. & Valentí, R. Revision of model parameters for κ -type charge transfer salts: An ab initio study. *Phys. Rev. Lett.* **103**, 067004 (2009). URL <https://link.aps.org/doi/10.1103/PhysRevLett.103.067004>.

[8] Hassan, N. M. *et al.* Melting of charge order in the low-temperature state of an electronic ferroelectric-like system. *npj Quantum Materials* **5**, 1–6 (2020). URL <https://doi.org/10.1038/s41535-020-0217-5>.

[9] Shimizu, Y., Miyagawa, K., Kanoda, K., Maesato, M. & Saito, G. Spin liquid state in an organic mott insulator with a triangular lattice. *Physical review letters* **91**, 107001 (2003). URL <https://link.aps.org/doi/10.1103/PhysRevLett.91.107001>.

[10] Yamashita, S. *et al.* Thermodynamic properties of a spin-1/2 spin-liquid state in a κ -type organic salt. *Nature Physics* **4**, 459–462 (2008). URL <http://www.nature.com/nphys/journal/v4/n6/full/nphys942.html>.

[11] Nakamura, Y. *et al.* Magnetic raman scattering study of spin frustrated systems, κ -(BEDT-TTF) $_2$ X. *Journal of the Physical Society of Japan* **83**, 074708 (2014). URL <https://doi.org/10.7566/JPSJ.83.074708>.

[12] Hassan, N. *et al.* Raman scattering as a probe of the magnetic state of BEDT-TTF based mott insulators. *Crystals* **8**, 233 (2018). URL <https://www.mdpi.com/2073-4352/8/6/233>.

[13] Shimizu, Y. *et al.* Pressure-tuned exchange coupling of a quantum spin liquid in the molecular triangular lattice κ -(ET) $_2$ Ag $_2$ (CN) $_3$. *Phys. Rev. Lett.* **117**, 107203 (2016). URL <https://link.aps.org/doi/10.1103/PhysRevLett.117.107203>.

[14] Aldoshina, M. *et al.* A new series of et-based organic metalls: synthesis, crystal structure and properties. *Synthetic metals* **56**, 1905–1909 (1993).

[15] Yamashita, M. *et al.* Ferromagnetism out of charge fluctuation of strongly correlated electrons in κ -(BEDTTF) $_2$ Hg(SCN) $_2$ Br. *npj Quantum Materials* **6**, 87 (2021). URL <https://doi.org/10.1038/s41535-021-00387-6>.

[16] Urai, M. *et al.* Anomalously field-susceptible spin clusters emerging in the electric-dipole liquid candidate κ -(ET) $_2$ Hg(SCN) $_2$ Br. *Science Advances* **8**, eabn1680 (2022). URL <https://www.science.org/doi/abs/10.1126/sciadv.abn1680>.

[17] Drichko, N. *et al.* Metallic state and charge-order metal-insulator transition in the quasi-two-dimensional conductor κ -(BEDT-TTF) $_2$ Hg(SCN) $_2$ Cl. *Phys. Rev. B* **89**, 075133 (2014). URL <https://link.aps.org/doi/10.1103/PhysRevB.89.075133>.

[18] Gati, E. *et al.* Evidence for electronically driven ferroelectricity in a strongly correlated dimerized BEDT-TTF molecular conductor. *Phys. Rev. Lett.* **120**, 247601 (2018). URL <https://link.aps.org/doi/10.1103/PhysRevLett.120.247601>.

[19] Hassan, N. M. *et al.* Probing the effect of mag-

- netic field on charge order in the quasi-two-dimensional mott insulator κ -(ET)₂Hg(SCN)₂Cl. *Phys. Rev. B* **104**, 245120 (2021). URL <https://link.aps.org/doi/10.1103/PhysRevB.104.245120>.
- [20] Blundo, E., Cappelluti, E., Felici, M., Pettinari, G. & Polimeni, A. Strain-tuning of the electronic, optical, and vibrational properties of two-dimensional crystals. *Applied Physics Reviews* **8**, 021318 (2021). URL <https://doi.org/10.1063/5.0037852>.
- [21] Kim, J. M. *et al.* Strain engineering of low-dimensional materials for emerging quantum phenomena and functionalities. *Advanced Materials* **35**, 2107362 (2023). URL <https://onlinelibrary.wiley.com/doi/abs/10.1002/adma.202107362>.
- [22] Schmidt, R. *et al.* Reversible uniaxial strain tuning in atomically thin WSe₂. *2D Materials* **3**, 021011 (2016). URL <https://dx.doi.org/10.1088/2053-1583/3/2/021011>.
- [23] Shin, B. G. *et al.* Indirect bandgap puddles in monolayer MoS₂ by substrate-induced local strain. *Advanced Materials* **28**, 9378–9384 (2016). URL <https://onlinelibrary.wiley.com/doi/abs/10.1002/adma.201602626>.
- [24] Zhao, C. *et al.* Strain tunable semimetal–topological-insulator transition in monolayer 1T'-WTe₂. *Phys. Rev. Lett.* **125**, 046801 (2020). URL <https://link.aps.org/doi/10.1103/PhysRevLett.125.046801>.
- [25] Lin, C. *et al.* Visualization of the strain-induced topological phase transition in a quasi-one-dimensional superconductor TaSe₃. *Nature Materials* **20**, 1093–1099 (2021). URL <https://doi.org/10.1038/s41563-021-01004-4>.
- [26] Cenker, J. *et al.* Reversible strain-induced magnetic phase transition in a van der waals magnet. *Nature Nanotechnology* **17**, 256–261 (2022). URL <https://doi.org/10.1038/s41565-021-01052-6>.
- [27] Böhmer, A. E. *et al.* Effect of biaxial strain on the phase transitions of Ca(Fe_{1-x}Co_x)₂As₂. *Phys. Rev. Lett.* **118**, 107002 (2017). URL <https://link.aps.org/doi/10.1103/PhysRevLett.118.107002>.
- [28] Hristov, A. T., Ikeda, M. S., Palmstrom, J. C., Walmsley, P. & Fisher, I. R. Elastoresistive and elastocaloric anomalies at magnetic and electronic-nematic critical points. *Phys. Rev. B* **99**, 100101 (2019). URL <https://link.aps.org/doi/10.1103/PhysRevB.99.100101>.
- [29] Malinowski, P. *et al.* Suppression of superconductivity by anisotropic strain near a nematic quantum critical point. *Nature Physics* **16**, 1189–1193 (2020). URL <https://doi.org/10.1038/s41567-020-0983-9>.
- [30] Ghini, M. *et al.* Strain tuning of nematicity and superconductivity in single crystals of FeSe. *Phys. Rev. B* **103**, 205139 (2021). URL <https://link.aps.org/doi/10.1103/PhysRevB.103.205139>.
- [31] Rubin, T., Altman, H. W. & Johnston, H. L. Coefficients of thermal expansion of solids at low temperatures. i. the thermal expansion of copper from 15 to 300°K. *Journal of the American Chemical Society* **76**, 5289–5293 (1954). URL <https://doi.org/10.1021/ja01650a009>.
- [32] See Supplemental Material at [URL will be inserted by publisher] for a detailed description of the fitting procedure, strain estimation from the sample, and crystallographic data.
- [33] Yamamoto, T. *et al.* Examination of the charge-sensitive vibrational modes in bis(ethylenedithio) tetrathiafulvalene. *The Journal of Physical Chemistry B* **109**, 15226–15235 (2005). URL <http://pubs.acs.org/doi/pdf/10.1021/jp050247o>.
- [34] Ivek, T. *et al.* Metal-insulator transition in the dimerized organic conductor κ -(BEDT-TTF)₂Hg(SCN)₂Br. *Phys. Rev. B* **96**, 085116 (2017). URL <https://link.aps.org/doi/10.1103/PhysRevB.96.085116>.
- [35] Naka, M. & Ishihara, S. Collective charge excitation in a dimer mott insulating system. *Journal of the Physical Society of Japan* **82**, 023701 (2013). URL <https://doi.org/10.7566/JPSJ.82.023701>.
- [36] Yao, N. Y., Zaletel, M. P., Stamper-Kurn, D. M. & Vishwanath, A. A quantum dipolar spin liquid. *Nature Physics* **1** (2018).
- [37] Jacko, A. C., Kenny, E. P. & Powell, B. J. Interplay of dipoles and spins in κ -(BEDT-TTF)₂X, where X = Hg(SCN)₂Cl, Hg(SCN)₂Br, Cu[N(CN)₂]Cl, Cu[N(CN)₂]Br, and Ag₂(CN)₃. *Phys. Rev. B* **101**, 125110 (2020). URL <https://link.aps.org/doi/10.1103/PhysRevB.101.125110>.
- [38] Koretsune, T. & Hotta, C. Evaluating model parameters of the κ - and β' -type mott insulating organic solids. *Phys. Rev. B* **89**, 045102 (2014). URL <https://link.aps.org/doi/10.1103/PhysRevB.89.045102>.

Supplementary Material: Tuning Charge Order in κ -(BED-TTF)₂Hg(SCN)₂X (X= Br, Cl) via Uniaxial Strain

Jesse Liebman,¹ Svetlana Torunova,² John A. Schlueter,³ Elena Zhilyaeva,² and Natalia Drichko¹

¹*Department of Physics and Astronomy, The Johns Hopkins University, Baltimore, Maryland 21218, USA*

²*Institute of Problems of Chemical Physics, Chernogolovka, Russia*

³*Division of Materials Research, National Science Foundation, Arlington, Virginia 22230, USA*

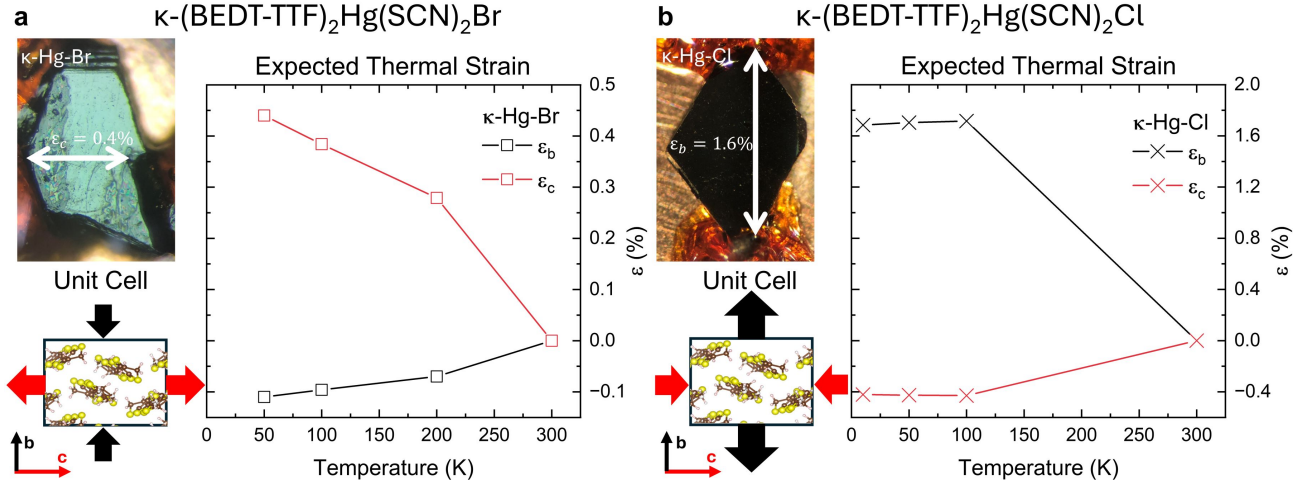


FIG. 1. Scheme for Application of Strain (a) κ -(BEDT-TTF) $_2$ Hg(SCN) $_2$ Br - the sample is glued along the c-axis on a copper substrate. The temperature dependence of expected thermal strain in κ -(BEDT-TTF) $_2$ Hg(SCN) $_2$ Br along the c-axis from gluing and b-axis from an estimated Poisson ratio of 0.25. (b) κ -(BEDT-TTF) $_2$ Hg(SCN) $_2$ Cl - the sample is glued along the b-axis on a copper substrate. The temperature dependence of expected thermal strain in κ -(BEDT-TTF) $_2$ Hg(SCN) $_2$ Cl along the b-axis from gluing and c-axis from an estimated Poisson ratio of 0.25

I. RAMAN SCATTERING MEASUREMENTS AND DATA ANALYSIS

Raman scattering spectra in the frequency range from 12 cm^{-1} to 2000 cm^{-1} and temperature range from 300 K down to 6 K were measured using the Jobin-Yvon T64000 Triple Monochromator Spectrometer equipped with a liquid Nitrogen cooled CCD. Line of Ar^+ - Kr^+ laser at 514.5nm was used for excitation. We performed macro-Raman Scattering Spectroscopy on samples of κ -Hg-Br and κ -Hg-Cl in a pseudo-Brewster angle geometry. We use a probe size of $100 \mu\text{m} \times 50 \mu\text{m}$ with a power of 1.5 mW, for which we estimate laser heating of less than 1.5 K. For the sample of κ -Hg-Cl we also performed micro-Raman Scattering Spectroscopy after one heating and cooling cycle. We focus incident light at 514.5 nm onto a beam spot of $2 \mu\text{m} \times 2 \mu\text{m}$ with a power of 0.060 mW, for which we estimate laser heating of less than 2 K. For low temperature measurement, samples were glued with GE varnish on a cold finger of a Janis ST500 Cryostat and cooled from 300 K to 5 K (3.5 K measured on the cold finger) using a cooling rate below 1 K/min. The crystals were oriented using by polarization dependent Raman Scattering Spectroscopy measurements. We measured with light incident along the a axis of the material in the (b,b) polarization for κ -Hg-Br and the (c,c) polarization for κ -Hg-Br, allowing us to probe modes in the A_g representation. For room temperature measurement, samples were glued on a Titanium platform with an effective length of 3.8 mm which propagated in-situ strain from a CS100 Razorbill Strain Cell¹.

To identify the electronic ground state, we use Raman Spectroscopy to measure the charge sensitive molecular vibration ν_2 . We fit features of molecular vibrations and lattice phonons using Voigt profiles, or a convolution of a Gaussian distribution with a Lorentzian profile:

$$I(\omega) \propto \int_{-\infty}^{\infty} d\omega' G(\omega', \omega, \sigma_{\text{res}}) L(\omega, \omega_i, \Gamma_i) \quad (1)$$

The σ_{res} parameter is the Gaussian spectral resolution parameter. For all measurements, this value is 2 cm^{-1} . ω_i is the frequency of vibration. Γ_i is the phenomenological damping factor, which is inversely proportional to the lifetime of a vibration². We fit each molecular vibration and lattice phonon individually and then fit all of the lineshape parameters over a frequency range of 200 cm^{-1} together with a linear background to approximate broad features, such as photoluminescence and soft mode of dipole fluctuations^{3,4}. For the charge sensitive molecular vibration ν_2 we use static and dynamic fits of a two-site model with fluctuations between the sites of frequency ω_{ex} . For the static case $\omega_{\text{ex}} = 0$ and we have independent Voigt profiles, defined by a splitting in frequency which is related to the charge separation Δn ⁵.

$$\Delta = \frac{120 \text{ cm}^{-1}}{1e^-} \Delta n \quad (2)$$

For the two-site model with fluctuations we use the phenomenological lineshape description provided in Ref.^{6,7}:

$$I(\omega) \propto \text{Re} \left[(a_1 \ a_2) \begin{pmatrix} i(\omega - (\omega_0 - \frac{\Delta}{2})) + \frac{\omega_{\text{ex}}}{2} + \Gamma_0/2 & -\frac{\omega_{\text{ex}}}{2} \\ -\frac{\omega_{\text{ex}}}{2} & i(\omega - (\omega_0 + \frac{\Delta}{2})) + \frac{\omega_{\text{ex}}}{2} + \Gamma_0/2 \end{pmatrix}^{-1} \begin{pmatrix} a_1 \\ a_2 \end{pmatrix} \right] \quad (3)$$

Where i is the imaginary unit. a_1 and a_2 are intensity prefactors for sites 1 and 2, respectively. ω_0 is the frequency of ν_2 where charge is equally shared between sites 1 and 2, and Γ_0 is the phenomenological damping constant of ν_2 . Δ is the splitting in frequency for each site and ω_{ex} is the frequency of fluctuations of charge between sites.

II. APPLICATION OF STRAIN

We applied uniaxial strain by using the difference in thermal contraction between the material, (see Tables I and II) and the Cu substrate⁸. We glued opposing ends of the crystal along each axis using GE varnish, as shown in Fig. 1. The applied strain is temperature dependent. As the Cu substrate cools to a temperature T , the change in the distance between the two glued ends L_0 is determined by the thermal contraction of Cu on cooling, $C_{\text{Cu}}(T)$.

$$L_0(T) = L_0(1 + C_{\text{Cu}}(T)) \quad (4)$$

As a sample of κ -Hg-X cools to a temperature T without strain, the change in the size of the sample along an axis i , $L_i^{(0)}$ is determined by the thermal contraction of the material, $C_{\text{X}, i}^{(0)}(T)$.

$$a_i^{(0)}(T) = L_i^{(0)}(1 + C_{\text{X}, i}^{(0)}(T)) \quad (5)$$

The applied strain on the sample of a material X, along an axis i , at each temperature, $\epsilon_{\text{X}, i}(T)$, can be determined as follows:

$$\epsilon_{\text{X}, i}(T) = \frac{\Delta L_i}{L_i^{(0)}} = C_{\text{Cu}}(T) - C_{\text{X}, i}^{(0)}(T) \quad (6)$$

where $\Delta L_i = L_0(T) - L_i^{(0)}(T)$ is the applied displacement along the axis i . Since Cu contracts less on cooling than samples of κ -Hg-X, $C_{\text{Cu}}(T) - C_{\text{X}, i}^{(0)}(T) > 0$ and we apply tensile strain. For X=Br, we apply a strain of 0.4% along the c -axis. For X=Cl, we apply a strain of 1.6% along the b -axis. While the strain is temperature dependent, we expect the strain to be roughly uniform below 100 K.

III. CRYSTALLOGRAPHIC INFORMATION

Temperature (K)	a (Å)	b (Å)	c (Å)	β (°)	V
100	36.7093	8.2015	11.6494	90.16	3507.3
200	36.8904	8.2619	11.6734	90.228	3557.9
300	37.0923	8.3278	11.7296	90.345	3623.2

TABLE I. Temperature dependence of the unit cell of κ -(BEDT-TTF)Hg(SCN)₂Br

Temperature (K)	a (Å)	b (Å)	c (Å)	β (°)	V
10	36.367	8.1209	11.741	90.186	3467.5
50	36.403	8.1226	11.7658	90.268	3478.9
100	36.2617	8.1222	11.7248	90.266	3453.2
300	36.5964	8.2887	11.7503	90.067	3564.2

TABLE II. Temperature dependence of the unit cell of κ -(BEDT-TTF)Hg(SCN)₂Cl⁹

Both κ -(BEDT-TTF)₂Hg(SCN)₂Br (κ -Hg-Br) and κ -(BEDT-TTF)₂Hg(SCN)₂Cl (κ -Hg-Cl) crystallize in the C2/c space group (No. 15). The temperature dependence of the unit cell parameters of κ -Hg-Br and κ -Hg-Cl is shown in Table I and Table II, respectively. The structural refinement of κ -Hg-Br at 100 K is given in Table III.

Atom	x	y	z	Occ.	U	Wyck. Pos.
Br(21)	0	0.7951	0.25	1	0.027	4e
C(1)	0.2656	0.5906	-0.08862	1	0.017	8f
C(2)	0.30105	0.5852	-0.05344	1	0.017	8f
C(3)	0.19721	0.5349	-0.12135	1	0.017	8f
C(4)	0.20716	0.6386	-0.20622	1	0.017	8f
C(5)	0.36303	0.4919	0.0279	1	0.018	8f
C(6)	0.37134	0.5977	-0.0571	1	0.02	8f
C(7A)	0.12742	0.5345	-0.2166	0.658	0.02	8f
C(7B)	0.12587	0.581	-0.166	0.342	0.02	8f
C(8A)	0.13729	0.7057	-0.2555	0.658	0.02	8f
C(8B)	0.13579	0.6113	-0.2906	0.342	0.02	8f
C(9A)	0.42869	0.5505	0.1219	0.789	0.02	8f
C(9B)	0.4328	0.5671	0.102	0.211	0.02	8f
C(10A)	0.44636	0.5888	-8E-4	0.789	0.02	8f
C(10B)	0.444	0.5825	0.0262	0.211	0.02	8f
C(21)	0.04443	0.4333	0.01737	1	0.024	8f
H(7AA)	0.1302	0.4599	-0.2829	0.658	0.024	8f
H(7AB)	0.1014	0.5338	-0.1948	0.658	0.024	8f
H(7BA)	0.1008	0.5362	-0.1631	0.342	0.024	8f
H(7BB)	0.1257	0.6869	-0.1251	0.342	0.024	8f
H(8AA)	0.1362	0.78	-0.1887	0.658	0.024	8f
H(8AB)	0.119	0.7432	-0.3123	0.658	0.024	8f
H(8BA)	0.1157	0.6727	-0.3276	0.342	0.024	8f
H(8BB)	0.1378	0.5049	-0.3302	0.342	0.024	8f
H(9AA)	0.4173	0.651	0.1523	0.789	0.024	8f
H(9AB)	0.4482	0.5173	0.176	0.789	0.024	8f
H(9BA)	0.4226	0.6734	0.1265	0.211	0.024	8f
H(9BB)	0.4523	0.5386	0.1571	0.211	0.024	8f
H(10A)	0.4592	0.49	-0.0281	0.789	0.024	8f
H(10B)	0.4648	0.676	0.0087	0.789	0.024	8f
H(10C)	0.4521	0.4746	-0.002	0.211	0.024	8f
H(10D)	0.4661	0.6504	0.0365	0.211	0.024	8f
Hg(21)	0	0.48924	0.25	1	0.022	4e
N(21)	0.04639	0.5111	-0.06526	1	0.031	8f
S(1)	0.2309	0.48233	-0.02106	1	0.018	8f
S(2)	0.25181	0.71141	-0.20397	1	0.02	8f
S(3)	0.31653	0.46982	0.06224	1	0.017	8f
S(4)	0.33466	0.69522	-0.1247	1	0.022	8f
S(5)	0.1542	0.45175	-0.09519	1	0.026	8f
S(6A)	0.18144	0.7183	-0.3181	0.658	0.018	8f
S(6B)	0.178	0.7234	-0.3115	0.342	0.032	8f
S(7A)	0.39503	0.39204	0.11446	0.789	0.019	8f
S(7B)	0.3935	0.4007	0.117	0.211	0.058	8f
S(8A)	0.41459	0.6505	-0.1079	0.789	0.024	8f
S(8B)	0.412	0.689	-0.1	0.211	0.032	8f
S(21)	0.04236	0.31689	0.13469	1	0.027	8f

TABLE III. Structural Refinement of κ -(BEDT-TTF)₂Hg(SCN)₂Br at 100 K. The numeric label associated with each atom denotes the corresponding carbon site which the atom is bonded to. The alphabetical label denotes the position of an atom in a given conformation. The relative abundance of each conformation is denoted by the occupancy.

IV. TREATMENT OF SPECTRA

The spectra are treated to remove photoluminescence (PL), which is treated as a broad background. The background and peak spectra are deconvoluted using an iterative modified polynomial fitting procedure¹⁰. The deconvolution was conducted with a polynomial of degree 7 and a convergence parameter of 10^{-4} . The scheme outlying this process is shown in Fig. 2. After deconvoluting all background features from vibrations, there are individual spectra for vibrations (Peak) and backgrounds (Back). The Peak spectra is fit to model all of the phonons, using a flat background. The fitted phonons are then subtracted from the Raw Spectra, which results in the Phonon Subtracted Spectra. In the Phonon Subtracted Spectra, broad features including collective dipole fluctuations and PL can be easily identified. The Phonon Subtracted Spectra are then fit in the high frequency region to fit the PL, which is then subtracted from the Raw Spectra. Finally, we have the PL subtracted spectra, where collective dipole fluctuations and vibrations can be examined independently of PL. For κ -Hg-Br this process is shown in Fig. 3. For κ -Hg-Cl this process is shown in Fig. 4. For both materials, the PL is characterized by a broad Lorentzian centered above 700 cm^{-1} , which is outside of the spectral window. We show each step in the process, from estimation of the background from the raw data to the final PL subtracted data.

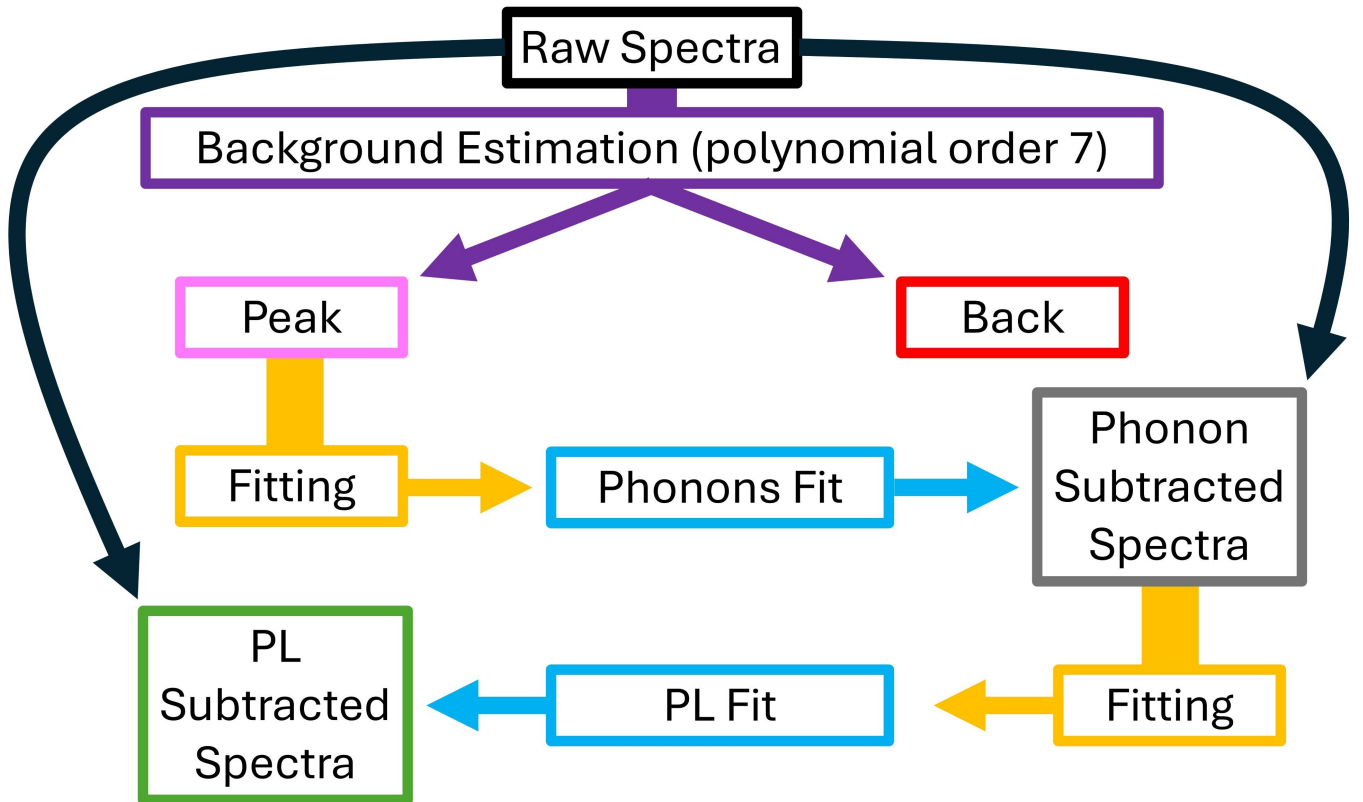


FIG. 2. Scheme for treatment of spectra using the iterative modified polynomial fitting, denoting each step taken from the raw spectra to the final PL subtracted spectra.

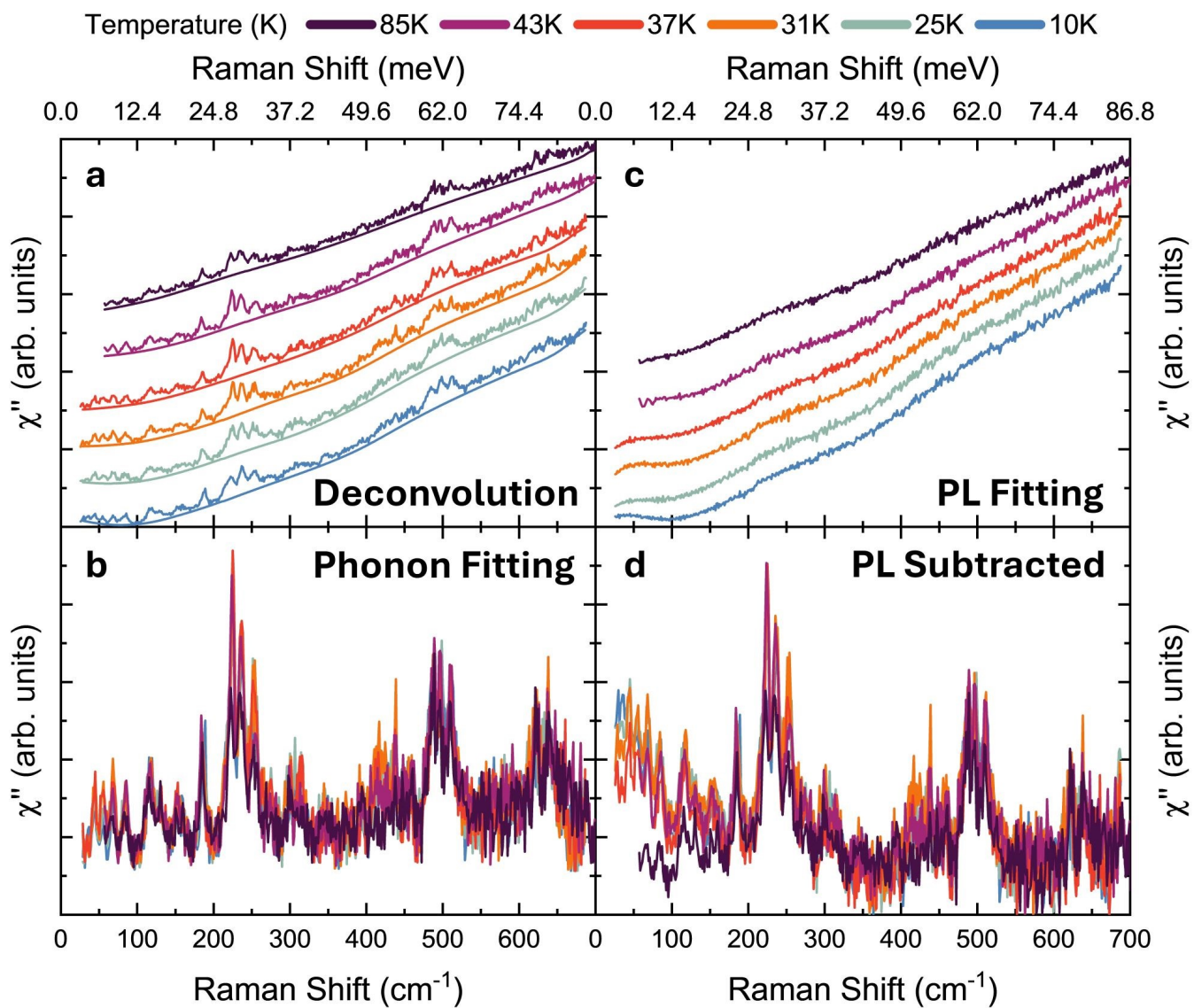


FIG. 3. Treatment of spectra of κ -(BEDT-TTF) $_2$ Hg(SCN) $_2$ Br. **a** Raw spectra, with estimated background for deconvolution. **b** Peak spectra used for Phonon Fitting. **c** Phonon Subtracted spectra used for PL fitting in the frequency range above 200 cm^{-1} . **d** Spectra with PL subtracted.

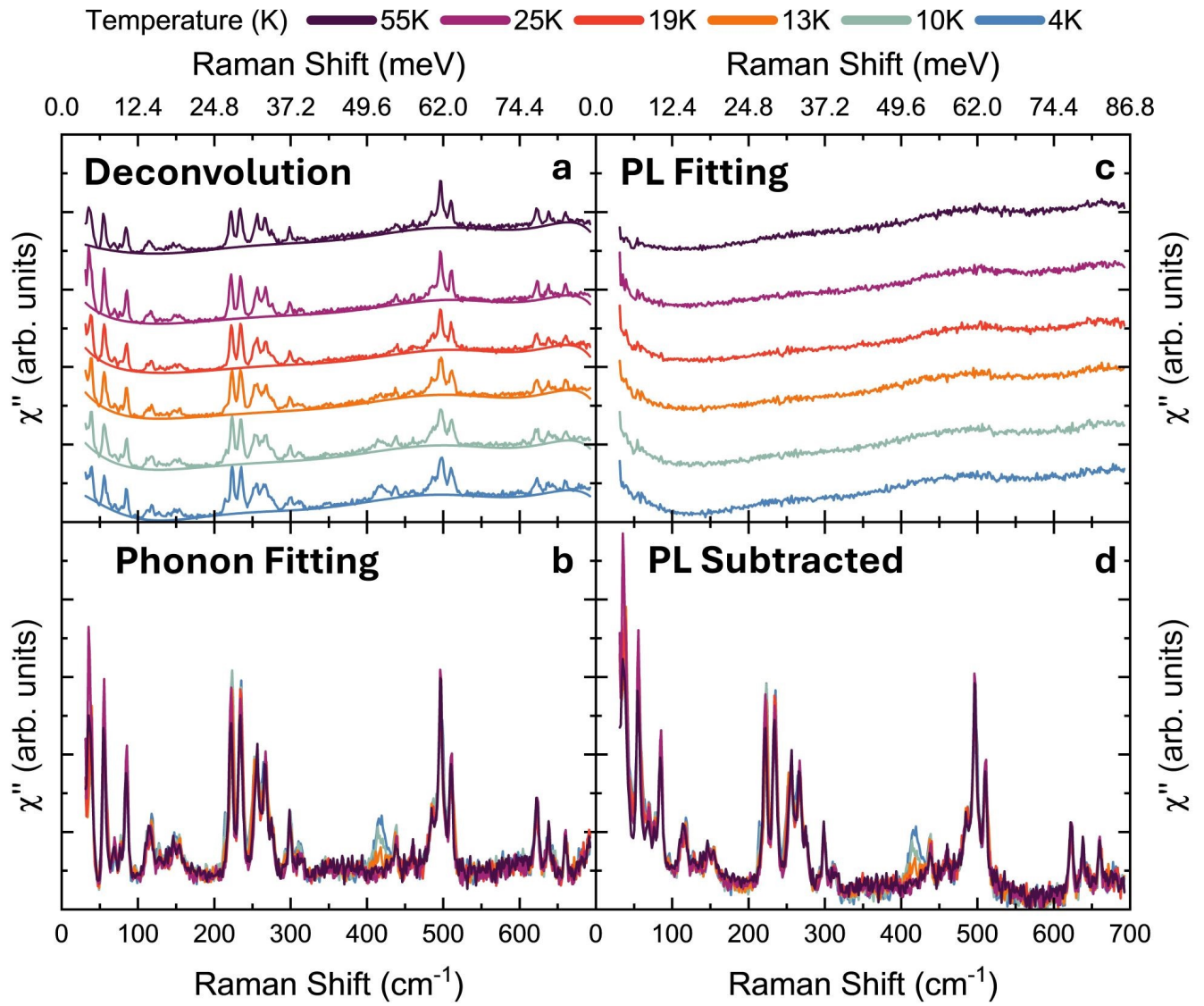


FIG. 4. Treatment of spectra of κ -(BEDT-TTF) $_2$ Hg(SCN) $_2$ Cl. **a** Raw spectra, with estimated background for deconvolution. **b** Peak spectra used for Phonon Fitting. **c** Phonon Subtracted spectra used for PL fitting in the frequency range above 200 cm^{-1} . **d** Spectra with PL subtracted.

V. ROOM TEMPERATURE STRAIN MEASUREMENTS

Room temperature strain measurements were performed on κ -Hg-Cl to determine the strain gauge factor of phonons. Strain was applied using a Razorbill CS100 Strain Cell through a Titanium platform¹. The sample was glued along the b-axis, so the applied strain would correspond to the applied strain in the low temperature measurements. Negative displacement or strain corresponds to compression, while positive displacement or strain corresponds to tension. We plot the spectra in Fig. 5a as a function of applied Voltage. Applied displacement was measured using the capacitance of the Razorbill CS100 Cell measured with a Keysight E4980AL LCR meter. Displacements up to $\pm 4.6\mu\text{m}$ were applied on an effective length of 3.4 mm, reaching strains of $\pm 0.135\%$. We use the fitted phonon frequency as a function of strain, which we estimate as linear. We plot the strain dependence of the frequency of the phonon near 115 cm^{-1} in Fig. 5b. Using a linear fit, we get a strain gauge factor of $(-10.6 \pm 4.6) \frac{\text{cm}^{-1}}{\%}$.

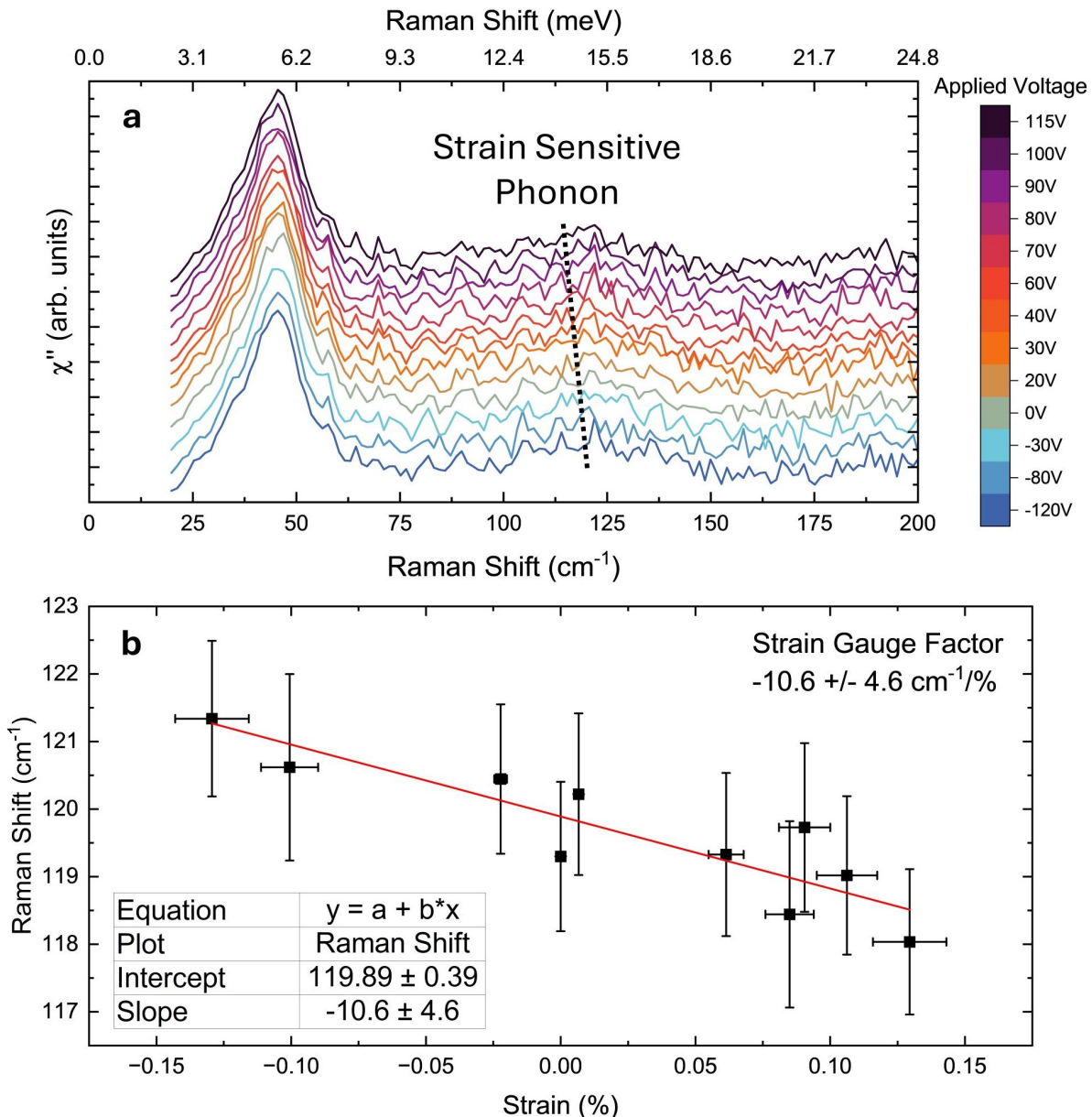


FIG. 5. Room Temperature measurements of the Raman spectra of κ -(BEDT-TTF)₂Hg(SCN)₂Cl under strain. **a** Spectra plotted as a function of strain. Spectra are shifted vertically for clarity. **b** Phonon Frequency plotted as a function of strain, with linear fit.

VI. TUNING OF HUBBARD PARAMETERS UNDER STRAIN

We now discuss the calculated tuning of the Extended Hubbard Model parameters under strain. As shown in Fig. 1, we calculate the expected strain given the difference in thermal contraction between the sample and the Cu substrate⁸. We also show the calculated lattice constants under strain in Fig. 1. We consider the Poisson Effect, which produces smaller strains along the other axes of the crystal. We assume the Poisson ratio to be roughly 0.25, which serves as a realistic estimate without direct measurement¹¹.

We use the calculated strain to estimate the leading order effects to be tuning of the parameters of the Extended Hubbard Model. In particular we predict the shift to intersite electron repulsion and intersite hopping, parameterized through V_{ab}^{ij} and t_{ab}^{ij} , respectively. We present the calculated Hubbard model parameters under strain in Fig. 6. For nearest neighboring interactions t, V , the interactions between sites a and b of different dimer sites are $V_{ab} = V_{ba}$, $t_{ab} = t_{ba}$, and between sites a and a or sites b and b are $V_{aa} = V_{bb}$, $t_{aa} = t_{bb}$. For the second nearest neighboring interactions t', V' , there is only interaction between inequivalent sites $V'_{ab} = V'_{ba}$, $t'_{ab} = t'_{ba}$. We use the following approximations for each Hubbard Model parameter, x , as a function of the applied strain ϵ :

$$\begin{aligned} x(\epsilon) &= \sum_{n=0} \epsilon^n \frac{d^n x}{d\epsilon^n} \Big|_{\epsilon=0} \\ &= x(0) + \epsilon \frac{dx}{d\epsilon} \Big|_{\epsilon=0} + O(\epsilon^2) \approx x_0 + \epsilon \frac{dx}{d\epsilon} \Big|_{\epsilon=0} \end{aligned} \quad (7)$$

For intersite repulsion, V_{ab}^{ij} , we expect the exact approximation of Eq. 7 holds:

$$V_{ab}^{ij}[\epsilon] = \frac{v_{ab}^{ij}}{r_{ab}^{ij}(1+\epsilon)} \approx \frac{v_{ab}^{ij}}{r_{ab}^{ij}}(1-\epsilon) = (1-\epsilon)(V_{ab}^{ij})[0] \quad (8)$$

For t_{ab}^{ij} , we make the following approximation:

$$\begin{aligned} t_{ab}^{ij}(\epsilon) &\propto \exp\left[-\frac{l_{ab}^{ij}(1+\epsilon)}{a_0}\right] \\ &\approx \exp\left[-\frac{l_{ab}^{ij}}{a_0}\right]\left(1-\epsilon\frac{l_{ab}^{ij}}{a_0}\right) = \left(1-\epsilon\frac{l_{ab}^{ij}}{a_0}\right)(t_{ab}^{ij})[0] \end{aligned} \quad (9)$$

where l_{ab}^{ij} is the unstrained intermolecular distance between molecules a, b in dimer sites i, j , and a_0 parameterizes the size of molecular orbitals in the tight binding approximation. For the approximated values in Fig. 6a and Fig. 6c, we let $\frac{l_{ab}^{ij}}{a_0} \approx 1$ when parameterizing $t_{ab}^{ij} = t_d$, the hopping between molecules in nearest-neighboring dimers. We also calculate the renormalization of $t_{ab}^{ij} = t_{ab}$, t'_{ab} , hopping between molecules from nearest and next-nearest neighboring dimers, respectively. In κ -Hg-Br, the intradimer distance is 3.6 Å and the interdimer distances are 7.1 Å and 8.3 Å¹². The structural refinement of κ -Hg-Br at 100K is provided in Table III. In κ -Hg-Cl, the intradimer distance is 3.5 Å and the interdimer distances are 7.1 Å and 8.1 Å¹³. Therefore, we expect the fraction $\frac{l_{ab}^{ij}}{a_0}$, and subsequent strain dependence is roughly twice as large for t_{ab} and t'_{ab} when compared to t_d . The ET molecules are oriented such that the long molecular axis and interatomic distances are mostly along the a -axis. We therefore expect a much smaller renormalization of U , so we allow all parameters other than the Hubbard U to be strain dependent.

VII. MONTE CARLO SIMULATION OF TRANSVERSE FIELD ISING MODEL

As discussed in the main text, emergent electric dipoles within $(\text{ET})_2^{1+}$ are mapped onto an $S = 1$ Transverse Field Ising Model (TFIM)¹⁴⁻¹⁶. We write the TFIM as follows:

$$\hat{H} = K_{\perp} \sum_i \hat{S}_i^x + \frac{1}{2} \sum_{i \neq j} K^{ij} \hat{S}_i^z \hat{S}_j^z \quad (10)$$

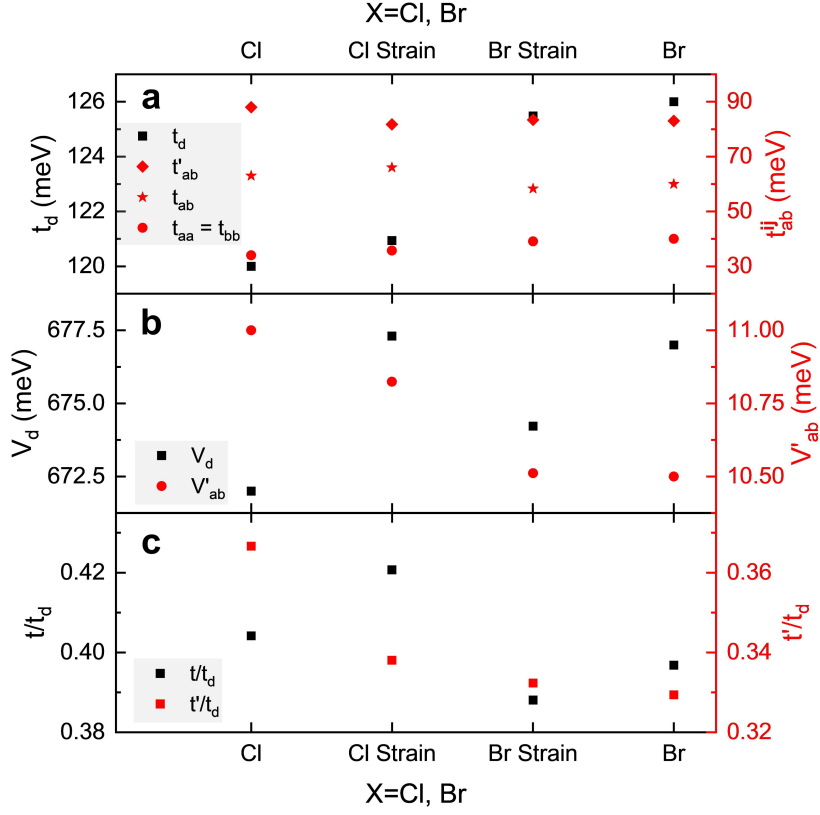


FIG. 6. Calculated tuning of interactions via strain in κ -(BEDT-TTF) $_2$ Hg(SCN) $_2$ X (X=Br, Cl). At maximal and constant strain below 50 K: (a) calculated intermolecular charge transfer integrals including intradimer charge transfer t_d (left axis) and interdimer monomer charge transfer t'_{ab} , t_{ab} , $t_{aa} = t_{bb}$ (b) intradimer electron repulsion and interdimer electron repulsion V'_{ab} (c) interdimer charge transfer integrals within the dimer approximation t , t' in units of t_d .

Following Ref.¹⁶, we use the following parameterization:

$$K_{\perp} = 2t_d \quad (11)$$

$$K^{ij} = D^{ij} + \tau^{ij} \quad (12)$$

$$D^{ij} = V_{aa}^{ij} + V_{bb}^{ij} - V_{ab}^{ij} - V_{ba}^{ij} \quad (13)$$

$$\tau^{ij} = \frac{(t_{ab}^{ij})^2 - (t_{aa}^{ij})^2}{V_d} - 8V_d \frac{(t_{ab}^{ij})^2 - (t_{aa}^{ij})^2}{D^2} \quad (14)$$

$$D = \frac{77V_d^2}{100} \quad (15)$$

In the notation used above, V_{aa}^{ij} refers to the Coulombic repulsion between molecular sites a and a between dimer lattice sites i and j and V_{ab}^{ij} refers to the Coulombic repulsion between molecular sites a and b between dimer lattice sites i and j . For hopping terms t , it is the same as V . To perform a Monte Carlo simulation, we rewrite the local state

$$|S_i\rangle = \sin \frac{\theta}{2} |+z\rangle + \cos \frac{\theta}{2} |-z\rangle = |\theta\rangle \quad (16)$$

This allows us to write a few observables:

$$\langle \hat{S}_x \rangle_\theta = \sin \theta \quad (17)$$

$$\langle \hat{S}_z \rangle_\theta = \cos \theta \quad (18)$$

$$\langle \hat{S}_x^2 \rangle_\theta = \sin^2 \theta \quad (19)$$

$$\langle \hat{S}_z^2 \rangle_\theta = \cos^2 \theta \quad (20)$$

We also can rewrite the Hamiltonian in terms of the value of θ at each lattice site i :

$$H = K_\perp \sum_i \sin \theta_i + \frac{1}{2} \sum_{i \neq j} K^{ij} \cos \theta_i \cos \theta_j \quad (21)$$

This approach allows us to perform a classical Monte Carlo simulation, where we can evaluate the expectation values of $\langle \hat{S}_x^2 \rangle$ and $\langle \hat{S}_z^2 \rangle$, which can differentiate between the dimer Mott and charge order phases. We use a 16×16 cluster with periodic boundary conditions and evaluate $\langle \hat{S}_z^2 \rangle$ at $T=0$ to identify the ground state for a wide selection of parameters for K_1 and K_2 in the range corresponding to the calculated parameterization of K_1 and K_2 in Ref¹⁶ and the calculated tuning of interactions via strain, shown in Fig. 6. We use $4 \times N^2 \times 1000 = 4 \times 16^2 \times 1000 = 1024000$ iterations to effectively sample an average 4000 values of θ for each of the 256 sites. At each iteration we use the following procedure:

1. Randomly sample a lattice site
2. Randomly choose a new value of $\theta \in [0, 2\pi)$
3. Calculate the difference between the current and new energies, $\Delta E = E_{\text{new}} - E_{\text{old}}$
4. If the new energy is lower ($\Delta E < 0$), accept the new value of θ . If not, choose a random number from 0 to 1 and see if this number is less than $\exp(-\Delta E\beta)$. For $T = 0$, an energy gain is always rejected.

At the end of the simulation, the expectation values, such as $\langle \hat{S}_z^2 \rangle$ are calculated.

-
- ¹ Park, J. *et al.* Rigid platform for applying large tunable strains to mechanically delicate samples. *Review of Scientific Instruments* **91**, 083902 (2020). URL <https://doi.org/10.1063/5.0008829>.
 - ² Klemens, P. G. Anharmonic decay of optical phonons. *Phys. Rev.* **148**, 845–848 (1966). URL <https://link.aps.org/doi/10.1103/PhysRev.148.845>.
 - ³ Hassan, N. *et al.* Evidence for a quantum dipole liquid state in an organic quasi-two-dimensional material. *Science* **360**, 1101–1104 (2018). URL <https://www.science.org/doi/abs/10.1126/science.aan6286>.
 - ⁴ Hassan, N. *et al.* Raman scattering as a probe of the magnetic state of BEDT-TTF based mott insulators. *Crystals* **8**, 233 (2018). URL <https://www.mdpi.com/2073-4352/8/6/233>.
 - ⁵ Yamamoto, T. *et al.* Examination of the charge-sensitive vibrational modes in bis (ethylenedithio) tetrathiafulvalene. *The Journal of Physical Chemistry B* **109**, 15226–15235 (2005). URL <http://pubs.acs.org/doi/pdf/10.1021/jp050247o>.
 - ⁶ Kubo, R. A stochastic theory of line shape. *Advances in Chemical Physics* **15**, 101–127 (1969). URL <https://onlinelibrary.wiley.com/doi/abs/10.1002/9780470143605.ch6>.
 - ⁷ Yakushi, K. Infrared and raman studies of charge ordering in organic conductors, BEDT-TTF salts with quarter-filled bands. *Crystals* **2**, 1291–1346 (2012). URL <https://www.mdpi.com/2073-4352/2/3/1291>.
 - ⁸ Rubin, T., Altman, H. W. & Johnston, H. L. Coefficients of thermal expansion of solids at low temperatures. i. the thermal expansion of copper from 15 to 300°K. *Journal of the American Chemical Society* **76**, 5289–5293 (1954). URL <https://doi.org/10.1021/ja01650a009>.
 - ⁹ Gati, E. *et al.* Evidence for electronically driven ferroelectricity in a strongly correlated dimerized BEDT-TTF molecular conductor. *Phys. Rev. Lett.* **120**, 247601 (2018). URL <https://link.aps.org/doi/10.1103/PhysRevLett.120.247601>.
 - ¹⁰ Zhao, J., Lui, H., McLean, D. I. & Zeng, H. Automated autofluorescence background subtraction algorithm for biomedical raman spectroscopy. *Appl Spectrosc* **61**, 1225–1232 (2007).
 - ¹¹ Greaves, G. N., Greer, A. L., Lakes, R. S. & Rouxel, T. Poisson’s ratio and modern materials. *Nature Materials* **10**, 823–837 (2011). URL <https://doi.org/10.1038/nmat3134>.
 - ¹² Aldoshina, M. *et al.* A new series of et-based organic metals: synthesis, crystal structure and properties. *Synthetic metals* **56**, 1905–1909 (1993).
 - ¹³ Konovalikhin, S. V. *et al.* Crystal structures of the organic metals (ET)₂[Hg(SCN)Cl₂] and (ET)₂[Hg(SCN)₂Br]. *Bulletin of the Russian Academy of Sciences, Division of chemical science* **41**, 1819–1826 (1992). URL <https://doi.org/10.1007/BF00863816>.
 - ¹⁴ Naka, M. & Ishihara, S. Electronic ferroelectricity in a dimer mott insulator. *Journal of the Physical Society of Japan* **79**, 063707 (2010). URL <https://doi.org/10.1143/JPSJ.79.063707>.
 - ¹⁵ Hotta, C. Quantum electric dipoles in spin-liquid dimer mott insulator κ -ET₂Cu₂(CN)₃. *Physical Review B* **82**, 241104(R) (2010). URL <https://link.aps.org/doi/10.1103/PhysRevB.82.241104>.
 - ¹⁶ Jacko, A. C., Kenny, E. P. & Powell, B. J. Interplay of dipoles and spins in κ -(BEDT-TTF)₂X, where X = Hg(SCN)₂Cl, Hg(SCN)₂Br, Cu[N(CN)₂]Cl, Cu[N(CN)₂]Br, and Ag₂(CN)₃. *Phys. Rev. B* **101**, 125110 (2020). URL <https://link.aps.org/doi/10.1103/PhysRevB.101.125110>.